

## Bayesian inference based parametric identification of vortex-excited force using on-site measured vibration data on a long-span bridge

Peng Liu <sup>a,b</sup>, Xiaolei Chu <sup>a,b</sup>, Wei Cui <sup>a,b,c,\*</sup>, Lin Zhao <sup>a,b,c,d</sup>, Yaojun Ge <sup>a,b,c</sup>

<sup>a</sup> State Key Lab of Disaster Reduction in Civil Engineering, Tongji University, Shanghai 200092, China

<sup>b</sup> Department of Bridge Engineering, College of Civil Engineering, Tongji University, Shanghai 200092, China

<sup>c</sup> Key Laboratory of Transport Industry of Wind Resistant Technology for Bridge Structures, Tongji University, Shanghai 200092, China

<sup>d</sup> State Key Laboratory of Mountain Bridge and Tunnel Engineering, Chongqing Jiaotong University, Chongqing, 400074, China



### ARTICLE INFO

**Keywords:**

Vortex-induced vibration  
Parametric identification  
Field monitoring  
Bayesian inference

### ABSTRACT

In recent years, vortex-induced vibration (VIV) events have occurred on several long-span suspension bridges around the world. Normally, the VIV of a long-span bridge is investigated in wind tunnel tests or computational fluid dynamics. However, examination of bridge VIV through full-scale field test data has rarely been conducted. Because of the rapid development of high precision sensors and high-frequency data transmission devices, the acquisition of structural modal information utilizing field test data from structural health monitoring systems is emerging as a powerful tool to explore the structural dynamic status and locate potential damage. Therefore, it is possible and necessary to inspect the bridge VEF (vortex-excited force) parameters from full-scale field test data and then to simulate and estimate the structural VIV response based on VEF parameters. Existing VEF parametric identification techniques allow structures (sectional model or full-scale bridges) to be tested under laminar flow in wind tunnel tests with known dynamic properties (inertial frequency and damping ratio), requiring measurement of responsive signals and VEF signals synchronously. However, for the actual field test of the full-scale bridge, the flow field is turbulent, and the structural responsive signal is unavoidably contaminated by measuring noises. Furthermore, it is impractical to synchronously record the aerodynamic force applied on the bridge deck during the field test. In this study, a Bayesian inference approach is introduced for the identification of VEF parameters using field vibration data. Using the fast Fourier transform (FFT) of field vibration data, a frequency domain formulation is proposed focusing on the structural vibration mode excited during VIV events. This method fully considers the influence of random vibration induced by ambient excitation and instrument measurement error on the field vibration data, and only the responsive data are needed without measuring the aerodynamic force information.

### 1. Introduction

With the improved levels of economic and technological development, innovative building and infrastructure structure design have become the main trend worldwide, resulting in high-rise buildings and long-span bridges [1] with significant structural flexibility. For long-span bridges, as the span becomes longer, the stiffness and damping decrease, thus greatly increasing their wind sensitivity [2]. They are more prone to violent oscillations when subjected to periodic wind excitation caused by vortices generated by bluff bodies, such as bridge decks. These oscillations are called vortex-induced vibrations (VIVs).

In recent years, the concern related to VIV has increased as VIV has occurred on several long-span bridges, such as Deer Isle Bridge in USA [3], Great Belt Bridge in Denmark [4], Yi Sun-sin Bridge in Korea [5], Xihoumen Bridge [6] and Humen Bridge [7] in China.

Although VIV normally caused small amplitude vibration and rarely causes structural damage and collapse, it can result in large displacements and cause discomfort to drivers even under low wind velocity conditions, and can potentially reduce the structural lifetime due to fatigue.

To establish a vortex-induced force model suitable for engineering applications, many semiempirical mathematical models are employed to simplify the complex fluid-structure interaction, such as the linear and nonlinear model proposed by Scanlan [8], the generalized Vander Pol model proposed by Larsen [9], an empirical nonlinear model with three order terms proposed by Zhu et al. [10], and the Volterra series based reduced-order model proposed by Wu et al. [11] and Xu et al. [12]. In short, many semiempirical models with different features for bridge VIV have been established. Employing the synchronous

\* Correspondence to: Tongji University, 207 Wind Engineering Building, 1239 Siping Road, Shanghai, 200092, China.

E-mail addresses: [1550008@tongji.edu.cn](mailto:1550008@tongji.edu.cn) (P. Liu), [xiaoleichu@tongji.edu.cn](mailto:xiaoleichu@tongji.edu.cn) (X. Chu), [cuiwei@tongji.edu.cn](mailto:cuiwei@tongji.edu.cn) (W. Cui), [zhaolin@tongji.edu.cn](mailto:zhaolin@tongji.edu.cn) (L. Zhao).

measurement of aerodynamic forces and bridge section motion in a wind tunnel or by CFD techniques, the parameters in semiempirical models can be determined by the conventional least square technique by directly fitting the vortex-induced force history [10].

However, the abovementioned models based on a 2-D sectional model in wind tunnel test cannot consider the effect of different Reynolds numbers, inflow turbulence characteristics, and aerodynamic coherence effects, which limits their application in the accurate prediction of real bridge vortex amplitudes.

Fortunately, existing data transmission networks and high-precision sensors enable real-time monitoring of the structure's operational status and wind environment on a full-scale model [13–15]. Many parametric identification approaches, such as the Ibrahim time-domain method (ITD) using generalized eigenvalue decomposition [16], the method based on wavelet transforms [17,18], and the unscented Kalman filter (UKF) approach considering the nonlinear dependence of self-excited forces [19], have been applied to modal parametric identification. The above methods perform well in identifying the dynamic properties of long-span bridges such as natural frequencies, damping ratios, and mode shapes [20]. However, studies on the investigation of the aerodynamic parameters of long-span bridges using on-site monitoring data have been rare. One of the typical characteristics of the measured data is the low signal-to-noise ratio (SNR) in the signal [21], which will introduce uncertainty in identifying the parameters.

Except for the above approach, the Bayesian system identification approach is another popular stochastic identification methodology for parameter inference of predefined mathematical models [22]. A Bayesian approach offers a powerful perspective for system identification that explicitly addresses uncertainty and provides a rigorous means for quantifying the uncertainty of parameters of interest in the presence of measured data [23]. Recent years have seen many Bayesian formulations in the area of system or modal identification [24] using ambient vibration data, including a time-domain Bayesian formulation [25], Bayesian spectral density approach [24,26,27] and Bayesian fast Fourier transform (FFT) approach [28–31].

In this study, a Bayesian inference approach is introduced for the identification of VEF parameters using field measurements of vibration data from a full-scale bridge. Using the FFT of field vibration data, a frequency domain formulation is proposed focusing on VIV excited modes. This method fully considers the influence of ambient excitation and instrument measurement error on the field vibration data, and only responsive data are need. Synchronized aerodynamic force data, which are difficult to measure on a constructed bridge, are not necessary. Numerical simulation and field-measured vibration data are used to verify the practical application of the method. The probabilistic correlation between VEF parameters and wind characteristics from measured VIV events is summarized. Finally, the vibration amplitudes calculated by the VEF parameters during different VIV events are compared against the measured amplitudes to examine the applicability of the proposed method in this study.

## 2. Vortex-excited force model

Two directions, coupled wake-oscillator models and single-degree-of-freedom (SDOF), have been introduced into the mathematical modeling of VIV. Coupled wake-oscillator models attempt to simulate the entirety of wake-body behavior and SDOF models are employed to provide a macroscopic estimate of the system response amplitude by solving the dynamic equation regarding details of the phenomenon. For the intention of predicting response amplitudes, SDOF models are sufficient for wind engineering applications [32]. The general form of such models can be given by

$$m(\ddot{x} + 2\xi\omega\dot{x} + \omega^2x) = F(x, \dot{x}, \omega_s t) \quad (1)$$

where  $m$  is the structural mass;  $x$  is the vertical displacement variable;  $\omega$  is the inertial circular frequency of structures;  $\xi$  is the structural damping ratio;  $F$  is the vortex-excited force (VEF), and  $\omega_s$  is the Strouhal

frequency. Some researchers [8,10,33] proposed semiempirical VEF models, which can be unambiguously converted into linear models and nonlinear models. The form of linear VEF models [8] is given as follows:

$$F = \frac{1}{2}\rho U^2 D \left[ Y_1(K) \frac{\dot{x}}{U} + Y_2(K) \frac{x}{D} + \frac{1}{2}C_L(K) \sin(\omega_s t + \psi) \right] \quad (2)$$

where  $\rho$  is the density of air;  $U$  is the mean wind speed;  $D$  is the characteristic length (deck width);  $Y_1$  defines the self-excited damping ratio;  $Y_2$  defines the aeroelastic stiffness;  $C_L$  defines a direct harmonic force at  $\omega_s$ ;  $K = U/fD$  is the reduced wind speed, and  $\psi$  is the phase angle between the displacement variable and harmonic force.

In contrast to the formulation of linear VEF models, the amplitude-dependent aerodynamic damping term  $\epsilon(K)$  is considered to modify the aeroelastic self-excited force, which can superiorly explain the self-limited amplitude. The classical nonlinear VEF models transform the traditional SDOF dynamic equation into a nonlinear differential equation, which makes it relatively difficult to estimate the aeroelastic parameters. In this study, linear VEF models are adopted since the VIV amplitude of a full-scale bridge is often much lower than that obtained by the 2-D sectional model applied in laminar flow wind tunnel tests [34,35], which is appropriate for providing the response amplitude. The verification of the linear VIV model will be presented in the following section.

For a continuous elastic model, such as long-span bridge, the general dynamic equation form of a linear system under a VEF can be written by:

$$\mathbf{M}\ddot{\mathbf{x}} + \mathbf{C}\dot{\mathbf{x}} + \mathbf{K}\mathbf{x} = \mathbf{F}(\mathbf{x}, \dot{\mathbf{x}}, \omega_s t) \quad (3)$$

For the long-span bridge excited by VIV, the structural response DOFs can be reduced to single generalized mode coordinates:

$$\mathbf{x}(t) = \int_{y=0}^L \boldsymbol{\varphi}_i(y) dy \eta_i(t) \quad (4)$$

where  $\eta_i(t)$  is the  $i$ -th modal displacement of the VIV,  $\boldsymbol{\varphi}_i$  is the  $i$ -th modal shape, and  $y$  is the coordinates along the bridge span. The normalization of mode shape  $\boldsymbol{\varphi}_i$  is determined by the measured degrees of freedom (DOFs) and will be defined in the next section.

The aerodynamic force along the bridge deck is

$$\mathbf{F} = \frac{1}{2}\rho U^2 D \left[ Y_1(K) \frac{\dot{\mathbf{x}}}{U} + Y_2(K) \frac{\mathbf{x}}{D} + \frac{1}{2}C_L(K) \sin(\omega_s t + \psi) \right] \quad (5)$$

where  $\psi$  is the purely phase vector of the VEF at different locations along the bridge span.

Rewriting Eq. (4) yields:

$$\begin{aligned} \mathbf{M}\ddot{\mathbf{x}} + \left[ \mathbf{C} - \frac{1}{2}\rho U D Y_1(K) \mathbf{I}_n \right] \dot{\mathbf{x}} + \left[ \mathbf{K} - \frac{1}{2}\rho U^2 Y_2(K) \mathbf{I}_n \right] \mathbf{x} \\ = \frac{1}{4}\rho U^2 D C_L(K) \sin(\omega_s t + \psi) \end{aligned} \quad (6)$$

Substituting Eq. (4) into Eq. (3),  $\eta_i(t)$  should satisfy:

$$\ddot{\eta}_i(t) + 2\tilde{\xi}_i\tilde{\omega}_i\dot{\eta}_i(t) + \tilde{\omega}_i^2\eta_i(t) = f_i(t) \quad (7)$$

where

$$\tilde{\omega}_i = \sqrt{\omega_i^2 - \frac{\rho U^2 Y_2(K) G_{\eta i}}{2m_i}} \quad (8)$$

$$\tilde{\xi}_i = \frac{\omega_i \xi_i}{\tilde{\omega}_i} - \frac{\rho U D Y_1(K) G_{\eta i}}{4m_i \tilde{\omega}_i} \quad (9)$$

$$G_{\eta i} = \int_0^L \boldsymbol{\varphi}_i^2(y) dy \quad (10)$$

and  $\omega_i$  is the  $i$ -th inherent frequency of the VIV excited mode,  $\xi_i$  is the  $i$ -th structural damping ratio,  $m_i$  is the  $i$ -th generalized mass,  $\tilde{\omega}_i$  is the  $i$ -th aerodynamic affected frequency,  $\tilde{\xi}_i$  is the  $i$ -th aerodynamic affected damping ratio, and  $f_i(t)$  is the  $i$ -th harmonic force.

The generalized harmonic force is derived as:

$$\begin{aligned} f_i(t) &= \frac{1}{m_i} \int_{y=0}^L \boldsymbol{\varphi}_i(y) \frac{1}{4} \rho U^2 D C_L(K) \sin[\omega_s t + \psi(y)] dy \\ &= \frac{\rho U^2 D C_L(K) L}{4m_i} \left[ \sin(\omega_s t) \int_0^1 \boldsymbol{\varphi}_i(v) \cos \psi(v) dv + \right. \\ &\quad \left. \cos(\omega_s t) \int_0^1 \boldsymbol{\varphi}_i(v) \sin \psi(v) dv \right] \\ &= \frac{\rho U^2 D \hat{C}_{L,i}(K) L}{4m_i} \sin(\omega_s t + \hat{\psi}) \\ &= f_i \sin(\omega_s t + \hat{\psi}) \end{aligned} \quad (11)$$

where  $v = y/L$ ,  $L$  is the bridge span length and  $\hat{\psi} = \arctan \frac{\int_0^1 \boldsymbol{\varphi}_i(v) \sin \psi(v) dv}{\int_0^1 \boldsymbol{\varphi}_i(v) \cos \psi(v) dv}$ . More importantly,  $\hat{C}_{L,i}(K)$  is the modal generalized lift coefficient defined as

$$\hat{C}_{L,i}(K) = C_L(K) \sqrt{\left( \int_0^1 \boldsymbol{\varphi}_i(v) \sin \psi(v) dv \right)^2 + \left( \int_0^1 \boldsymbol{\varphi}_i(v) \cos \psi(v) dv \right)^2} \quad (12)$$

One point that needs to be clarified is that currently there is not enough data for quantifying the phase function of the vortex-shedding force. Therefore  $\psi(y)$  is unknown, and  $\hat{C}_{L,i}(K)$  is identified as a whole rather than to identify  $C_L$  directly. In other words, the harmonic force coefficient  $\hat{C}_{L,i}(K)$  in a long-span bridge comprehensively considers the vortex coherence along the bridge span, which is different from the one represented in the single degree of freedom VEF model as in Eq. (2).

Taking the Fourier transform for Eq. (7) gives:

$$(1 - 2i\xi_i \tilde{\omega}_i \omega_k^{-1} - \tilde{\omega}_i^2 \omega_k^{-2}) b_k = f_i F(\sin(\omega_s t + \hat{\psi})) \quad (13)$$

where  $b_k$  denotes the frequency response of  $\ddot{\eta}_i(t)$  at  $\omega_k$  and  $F(\cdot)$  denotes the Fourier transform coefficient of  $\sin(\omega_s t + \hat{\psi})$  at  $\omega_k$ . Therefore, the frequency response  $b_k$  at  $\omega_k$  is determined to be:

$$b_k = f_i (1 - 2i\xi_i \tilde{\omega}_i \omega_k^{-1} - \tilde{\omega}_i^2 \omega_k^{-2})^{-1} F(\sin(\omega_s t + \hat{\psi})) \quad (14)$$

### 3. Bayesian FFT parametric identification

#### 3.1. Negative log-likelihood function

Because of the oscillation of a linear system with  $n$  degrees of freedom (DOF) under VEF and considering the ambient vibration caused by the low turbulence field flow [36] or the action of other unknown environmental loads, the measured (i.e. acceleration) data  $\ddot{\mathbf{y}}_j \in R^n$  ( $j = 1, \dots, N$ ,  $N$  is the number of measuring samples,  $n$  is the number of measured DOFs) include three parts. The first part is the forced or self-excited vibration content VIV responses  $\ddot{\mathbf{x}}_{Fj}$  due to the self-excited force and periodic harmonic force. The second part is the ambient vibration responses  $\ddot{\mathbf{x}}_{aj}$  due to unknown environmental loads (e.g., turbulence-induced buffeting and vehicle-induced vibration). The third part is the prediction error  $\epsilon_j$  [29]

$$\ddot{\mathbf{y}}_j = \ddot{\mathbf{x}}_{Fj} + \ddot{\mathbf{x}}_{aj} + \epsilon_j \quad (15)$$

where  $N$  is the number of sampling points per channel. The FFT of  $\ddot{\mathbf{y}}_j$  is defined as

$$\begin{aligned} \mathbf{F}_k &= \text{Re}\mathbf{F}_k + i\text{Im}\mathbf{F}_k \\ &= \sqrt{\frac{2\Delta t}{N}} \sum_{j=1}^N \ddot{\mathbf{y}}_j \exp \left[ -2\pi i \frac{(k-1)(j-1)}{N} \right] \quad (k = 1, \dots, N) \end{aligned} \quad (16)$$

where  $i^2 = -1$ ;  $\Delta t$  is the sampling interval. For  $k = 2, 3, \dots, N_q$ , the FFT corresponds to frequency  $f_k = (k-1)/N\Delta t$ , where  $N_q = \text{int}[N/2] + 1$

(int[.] denotes the integer part) is the frequency index at the Nyquist frequency. Let

$$\mathbf{Z}_k = \begin{bmatrix} \text{Re}F_k \\ \text{Im}F_k \end{bmatrix} \in R^{2n} \quad (17)$$

where  $n$  is the number of measured DOFs.

The VIV phenomenon is usually manifested as single-mode participation, which is typical single-frequency vibrations. The modes are well-separated, and one can select a frequency band that is determined by a single mode of VIV. Due to the limited number of accelerometer devices, the excited mode shape  $\boldsymbol{\varphi}_i(y)$  is reduced to a vector  $\boldsymbol{\varphi}_i$  with  $n$  components. In the following part, the subscript  $i$  is omitted for brevity.

Using the VEF model mentioned by Section 2 and assuming that the dynamic properties ( $\omega$ ,  $\xi$  and  $\boldsymbol{\phi}$ ) of the structure are known in advance, let  $\theta$  denote the parameters to be identified, which includes five parameters  $\{\tilde{\omega}, \tilde{\xi}, \hat{C}_L, S, S_e\}$  and can be divided into three groups. The first group is  $\{\tilde{\omega}, \tilde{\xi}\}$ , where  $\tilde{\omega}$  and  $\tilde{\xi}$  denote aerodynamically affected circular frequency and aerodynamically affected damping ratio, respectively. The VEF parameters  $Y_1$  and  $Y_2$  can be solved by Eqs. (8) and (9). The second is  $\hat{C}_L$ , the modal generalized lift coefficient, which considers the vortex coherence along the bridge span. The third is  $S$ , the power spectral density (PSD) of modal forces of ambient excitation. The fourth is  $S_e$ , the (constant) PSD of prediction error (assuming the prediction error as independent and identically distributed (i.i.d.) Gaussian white noise). The assumptions for the PSD of the modal force and the PSD of the prediction error can be found in the literature [30,37,38].

For a given  $\theta$ , the VIV response  $\ddot{\mathbf{x}}_{Fj}(\theta)$  can be determined and hence is fixed. Then, referring to Eq. (15), the difference  $\ddot{\mathbf{y}}_j - \ddot{\mathbf{x}}_{Fj}(\theta)$  is distributed as the ambient vibration response with prediction error, whose statistical properties (PSD) have been described by  $S$  and  $S_e$ . For a fixed  $\theta$ , the difference  $\ddot{\mathbf{y}}_j - \ddot{\mathbf{x}}_{Fj}(\theta)$  is a zero-mean stationary stochastic process, where for large  $N$ , the FFT of  $\{\mathbf{Z}_k\}$  is asymptotically independent and each  $\{\mathbf{Z}_k\}$  has a Gaussian distribution with mean  $\mu_k(\theta)$  covariance matrix  $\mathbf{C}_k(\theta)$  given in terms of the FFT of modal correlation functions. In applications, only the FFTs on a selected resonant frequency band covering the vortex-induced models of interest are used for vortex-induced parameter identification. Choosing a noninformative prior distribution, the posterior probabilistic density distribution (PDF) of  $\theta$  given the measured signal is proportional to the likelihood function  $p(\{\mathbf{Z}_k\}|\theta)$ . Using Bayes' theorem, the posterior PDF of  $\theta$  is given by:

$$p(\theta|\{\mathbf{Z}_k\}) = \frac{p(\theta)p(\mathbf{Z}_k|\theta)}{p(\mathbf{Z}_k)} \propto p(\{\mathbf{Z}_k\}|\theta) \quad (18)$$

According to the distribution of  $\{\mathbf{Z}_k\}$  given  $\theta$ , the “negative log-likelihood function” (NLLF) can be given:

$$\begin{aligned} L(\theta) &= -\ln p(\{\mathbf{Z}_k\}|\theta) \\ &= n N_f (\ln 2 + \ln \pi) + \frac{1}{2} \sum_k \ln \det \mathbf{C}_k(\theta) \\ &\quad + \frac{1}{2} \sum_k [\mathbf{Z}_k - \mu_k(\theta)]^T \mathbf{C}_k(\theta)^{-1} [\mathbf{Z}_k - \mu_k(\theta)] \end{aligned} \quad (19)$$

where  $N_f$  is the number of FFT frequency points among resonant frequency band and  $\det[\cdot]$  denotes calculating the determinant.

$\mu_k(\theta)$  is the Fourier transform of VIV response  $\ddot{\mathbf{x}}_{Fj}(\theta)$ . Referring to Eq. (14), the  $\mu_k(\theta)$  is obtained as:

$$\mu_k(\theta) = \begin{bmatrix} \boldsymbol{\phi} b_{Rk} \\ \boldsymbol{\phi} b_{Ik} \end{bmatrix} \in R^{2n} \quad (20)$$

where  $b_{Rk}$  and  $b_{Ik}$  denote the real and imaginary parts of  $b_k$ , respectively.

The derivation of covariance matrix  $\mathbf{C}_k(\theta)$  can be referred to [29,39] and shown to be

$$\det \mathbf{C}_k(\theta) = 2^{-2n} [(SD_k/S_e + 1)S_e^n]^2 \quad (21)$$

$$\mathbf{C}_k^{-1}(\theta) = 2 \begin{bmatrix} S_e^{-1} \mathbf{I}_n - S_e^{-1} (1 + S_e/SD_k)^{-1} \boldsymbol{\phi} \boldsymbol{\phi}^T & \mathbf{0} \\ \mathbf{0} & S_e^{-1} \mathbf{I}_n - S_e^{-1} (1 + S_e/SD_k)^{-1} \boldsymbol{\phi} \boldsymbol{\phi}^T \end{bmatrix} \quad (22)$$

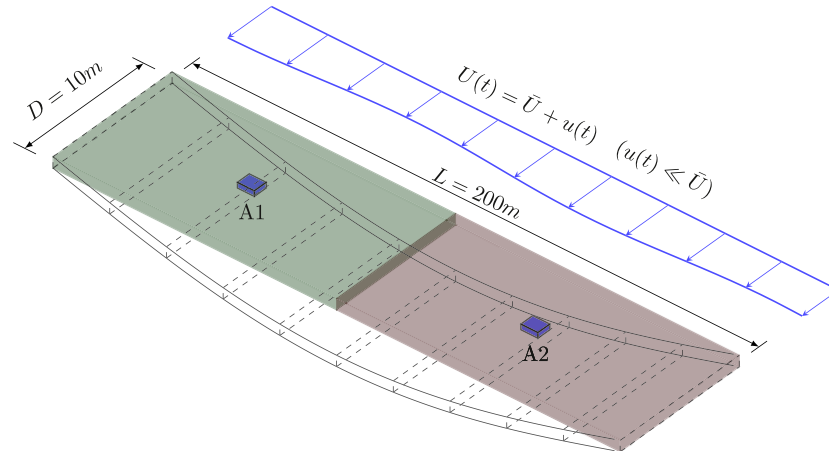


Fig. 1. Numerical simulation model with 2 measured DOFs (A1 denotes the No. 1 accelerometer and A2 denotes the No. 2 accelerometer).

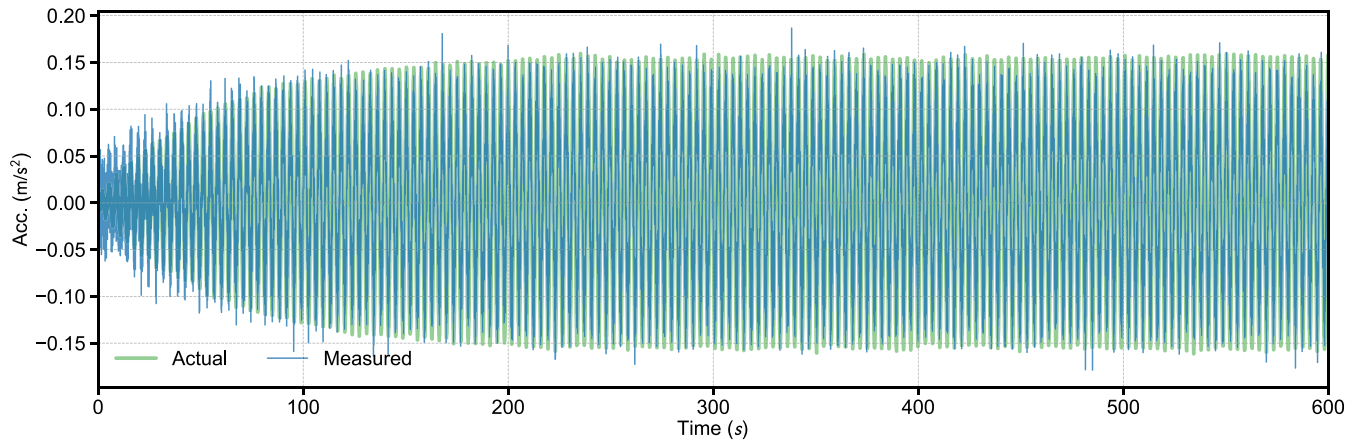


Fig. 2. Numerical simulation time history on time domain.

where

$$D_k(f, \xi) = [(\beta_k^2 - 1)^2 + (2\xi\beta_k)^2]^{-1} \quad (23)$$

$$\beta_k = \tilde{\omega}/(2\pi f_k) \quad (24)$$

and  $f_k$  is the FFT frequency abscissa of  $y_j$  shown in Eq. (16).

Substituting Eq. (20), Eq. (21) and into Eq. (19), and normalizing the modes shape as  $\phi^T \phi = 1$ :

$$\begin{aligned} L(\theta) = & nN_f \ln \pi + (n-1)N_f \ln S_e + \sum_k \ln(SD_k + S_e) \\ & + S_e^{-1} [d - \phi^T A \phi + \sum_k (1-a_k)(b_{Rk}^2 + b_{Ik}^2)] \\ & - 2\phi^T \sum_k (1-a_k)(b_{Rk} \operatorname{Re} F_k + b_{Ik} \operatorname{Im} F_k) \end{aligned} \quad (25)$$

where

$$a_k = (1 + S_e/SD_k)^{-1} \quad (26)$$

$$d = \sum_k (\operatorname{Re} F_k^T \operatorname{Re} F_k + \operatorname{Im} F_k^T \operatorname{Im} F_k) \quad (27)$$

$$A = \sum_k a_k (\operatorname{Re} F_k \operatorname{Re} F_k^T + \operatorname{Im} F_k \operatorname{Im} F_k^T) \quad (28)$$

The most probable values (MPVs) of  $\theta$  maximizes the posterior PDF, and hence minimizes the NLLF. The covariance matrix can be obtained by solving the inverse of the Hessian matrix at the MPV [31].

#### 4. Verification by numerical simulation

Consider a simply supported bridge with a main span ( $L = 200$  m) and the deck section width ( $D = 10$  m). The layout of the bridge deck is plotted in Fig. 1. The dynamic characteristics and relevant vortex-induced parameters are listed in Table 1. There are two measured degrees of freedom which can represent two modes, namely, a 1st symmetric vertical bend and a 1st antisymmetric vertical bend. The inherent circular frequency of the 1st symmetric vertical bend is 1.8028 rad/s, and the corresponding modal damping ratio is 0.03. The first-order symmetric vertical bending vortex-induced vibration occurs at the bridge under the mean wind speed  $\bar{U} = 8$  m/s is assumed. The coefficients of the self-excited damping ratio and aerodynamic stiffness are  $Y_1 = 0.6$  and  $Y_2 = 1$ , respectively, and the harmonic force coefficient  $\hat{C}_{L,1}$  is 3.

The incoming flow in the actual scene is usually accompanied by some turbulence, even when VIV events occur. In the numerical simulation, this part of the fluctuating wind load is considered as a Gaussian white noise process. The numerical simulation time history of the first measured point considering the simulation time history of VIV with Gaussian white noise excitation and prediction errors is plotted in Fig. 2 with sampling frequency of 100 Hz. The signal-noise ratio (SNR) between the measured signal and the real signal is 20 dB.

Using the Bayesian FFT parametric identification method mentioned in Section 3, the recognition result is shown in Fig. 3. The optimal parameters ( $\theta$ ) include  $\tilde{\omega}$ ,  $\xi$ ,  $\hat{C}_{L,1}$ ,  $S$  and  $S_e$ . The identification results of the VEF parameters are shown in Table 2. Given the identified values

**Table 1**

Dynamic properties and relevant vortex-induced parameters for numerical simulation.

Items	Values
Inherent frequency (rad/s)	1.8028 (SV) 2.1794 (ASV)
Structural damping ratio	0.03 (SV) 0.03 (ASV)
$Y_1$	0.6
$Y_2$	1.0
$\hat{C}_{L,1}$	3.0

**Table 2**

Identification results of VEF parameters under numerical simulation.

Items	$\bar{\omega}$ (rad/s)	$\tilde{\xi}$ (%)	$\hat{C}_{L,1}$
Real values ( $\theta$ )	1.7754	0.98	3.0000
Estimate values ( $\hat{\theta}$ )	1.7754	1.03	2.9848
( $ \theta - \hat{\theta} /\theta$ ) (%)	0.00	5.10	0.67
$\sigma$	0.0006	0.19	0.5470

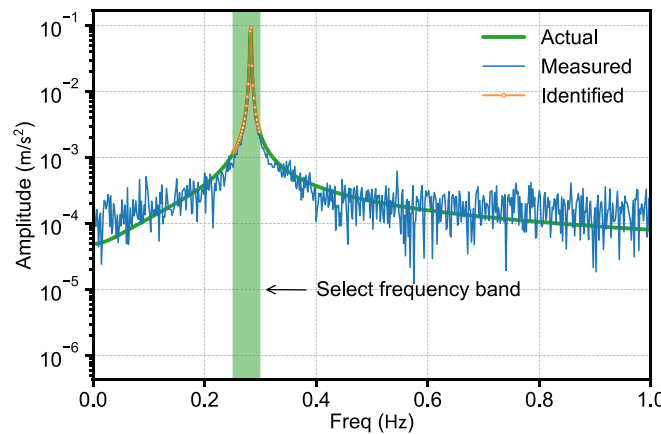


Fig. 3. Numerical simulation results on frequency spectrum.

of  $\bar{\omega}$ ,  $\tilde{\xi}$  and  $\hat{C}_{L,1}$ , the estimation error from the true value is very small, the VEF parameter  $Y_1$  is computed to be 0.5842, and  $Y_2$  is computed to be 1.0011. The posterior covariance values in Table 2 reflect the uncertainty associated with the dynamic characteristics given the FFT in the context of the empirical model used [27]. The c.o.v. values of parameters are of different orders of magnitude. The c.o.v. value of the aerodynamically affected circular frequency is significantly less than the aerodynamically affected damping ratio and generalized lift coefficient, which indicates that the former is identified with high accuracy.

## 5. Engineering application

### 5.1. Background information

The target bridge, Humen Bridge, is located at the sea gate of the Pearl River along the southern coastline of China. The coordinates are 22.791°N, 113.615°E, as shown in Fig. 4.

Humen Bridge is a suspension bridge with an 888 m main span. The sag to span ratio of the main cable is 1/10.5, and the two ends of the main cable are fixed by tunnel anchorages. There are a total of 72 pairs of hangers with 12 m between them. The elevation view of Humen Bridge is plotted in Fig. 5.

The streamlined closed box grid is used as the bridge deck section with 35.6 m width and 2.99 m depth. The detailed geometries of the bridge cross-section are illustrated in Fig. 6.

An unexpected VIV occurred on Humen Bridge starting from May 5th, 2020. To monitor the status of Humen Bridge, a health monitoring



Fig. 4. Geographic location of the target bridge.

system was added to the bridge and began to fully operate on June 9th, 2020. The wind records and acceleration signal were obtained afterward.

To better understand the mechanism of the VEF, the Bayesian FFT approach introduced in this study for parametric identification of the VEF was introduced to explore this VIV event using the measured data from June 9th, 2020 to July 20th, 2020 on Humen Bridge.

### 5.2. Field measured data description

The structural health monitoring system on Humen Bridge includes three-dimensional anemometers and a unidirectional accelerometer. The anemometers are used for wind-speed monitoring at a sampling frequency  $f_s = 4$  Hz (green points shown in Fig. 7). On the middle main span, one group of 3-dimensional anemometers are set on both sides of the flow to avoid aerodynamic interference. The incoming flow always carries fluctuating wind speed, and the measured wind speed  $U(t) = \bar{U} + u(t)$  where  $\bar{U}$  is the 10-min mean wind speed, even in VIV events. Seven sections (each eighth point) are selected for vertical bending and torsion vibration monitoring, and a total of 14 unidirectional accelerometers (vertical only) are arranged with sampling frequency  $f_s = 50$  Hz. The sensor layout is shown in Fig. 7.

#### 5.2.1. Wind characteristics general description

The wind characteristics include the 10-min mean wind speed, 10-min mean wind direction, and along-wind turbulence intensity when considering the VIV occurrence condition. The mathematical definition of the turbulence intensity of along-wind fluctuating wind speeds is as follows:

$$I_u = \frac{\sigma_u}{\bar{U}} \quad (29)$$

where  $\sigma_u$  is the standard deviation of the along-wind speed. Two anemometers are deployed to monitor the wind environment upstream and downstream of the river, named UA1 and UA2 respectively. To eliminate the influence of attached components on recording gust wind speed, the data collected by UA1 are only used when the wind direction is between 240° and (360 + 60)°. The data collected by UA2 are only used when the wind direction is between 60° and 240°. The wind-rose during June 9th, 2020 to July 20th, 2020 is plotted in Fig. 8. Due to the topography of the bridge site (see Fig. 4), the incoming flow during this time was mostly from the southern open sea terrain and the 10-min mean wind speed was mainly distributed from 4 m/s to 8 m/s. The low turbulence intensity of the incoming flow is one of

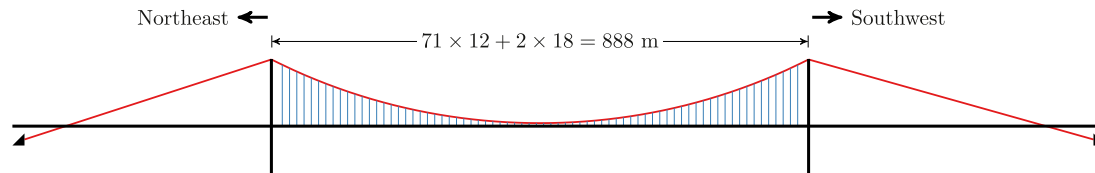


Fig. 5. Elevation view of Humen Bridge geometries.

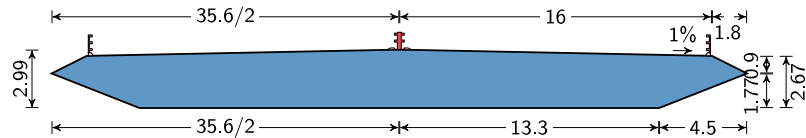


Fig. 6. Cross-section of Humen Bridge deck (unit: m).

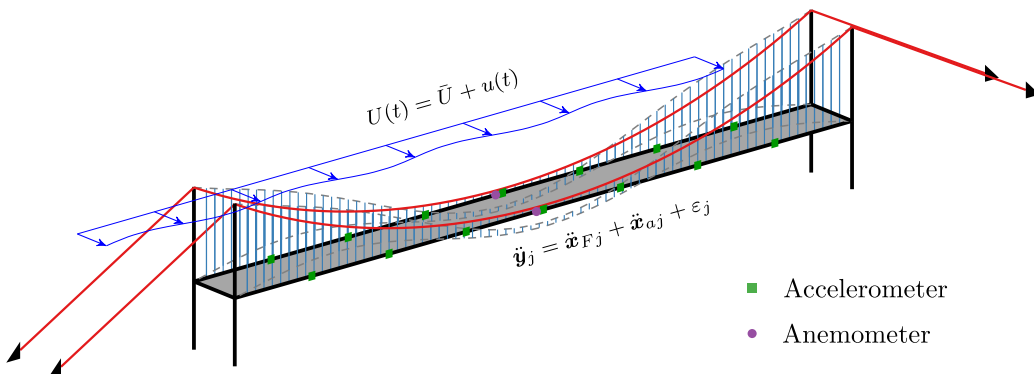


Fig. 7. Humen Bridge sensor layout and typical VIV modal shape.

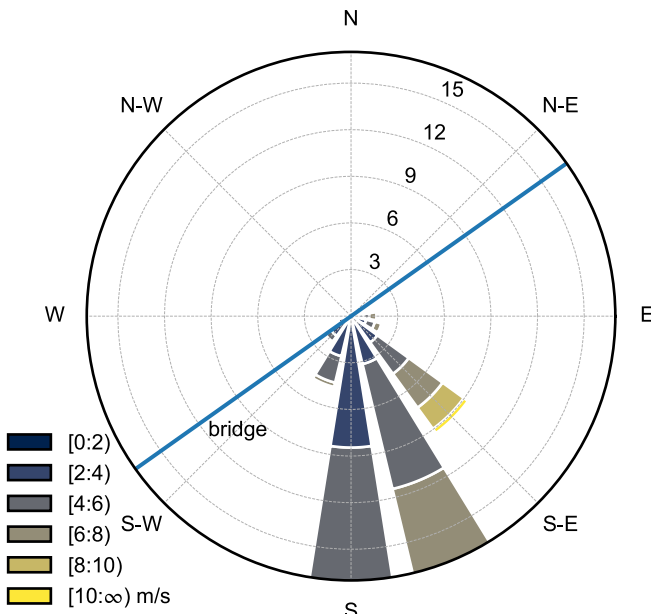


Fig. 8. Windrose at Humen Bridge site from June 9th to July 20th, 2020.

the key factors affecting the occurrence of VIV events. Fig. 9 shows the scatters between the mean wind speed and along-wind turbulence intensity during the monitoring period.

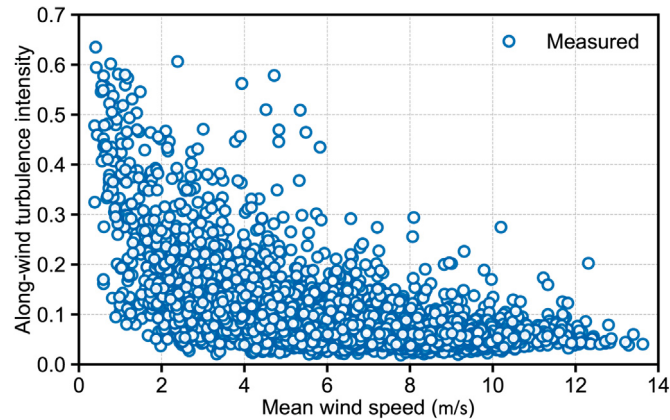


Fig. 9. Scatters between mean wind speed and along-wind turbulence intensity from June 9th to July 20th, 2020.

### 5.2.2. Vortex-induced vibration segment classification

Before identifying the parameters of the VEF, the VIV event should be separated to avoid the effect of other vibration events (e.g., vehicle-induced vibration and buffeting) from the full acceleration signals. Vehicle-induced vibration and buffeting are typical broadband stochastic processes with multiple modes. However, VIV is an aerodynamic phenomenon with strong interaction between wind and bridge deck, which is induced by vortex shedding periodically around the bridge at the lock-in wind speed interval. The self-excited vibration of the bridge deck is also involved in the vibration development. The vortex shedding frequency is generally proportional to the velocity according to the

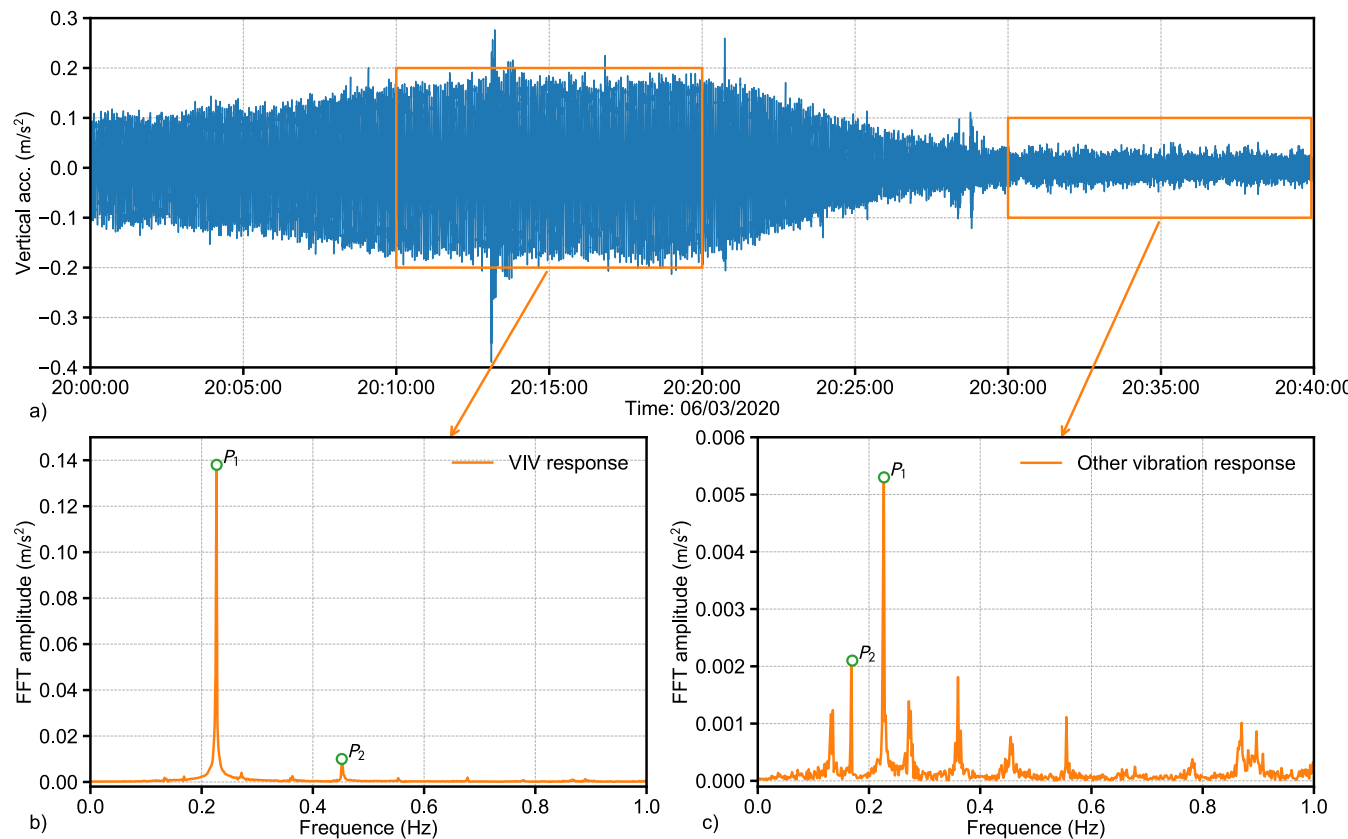


Fig. 10. Vertical acceleration characteristic of bridge deck under VIV or other vibrations (a) time history of vibration, (b) FFT spectrum of VIV event, (c) FFT spectrum of other vibration.

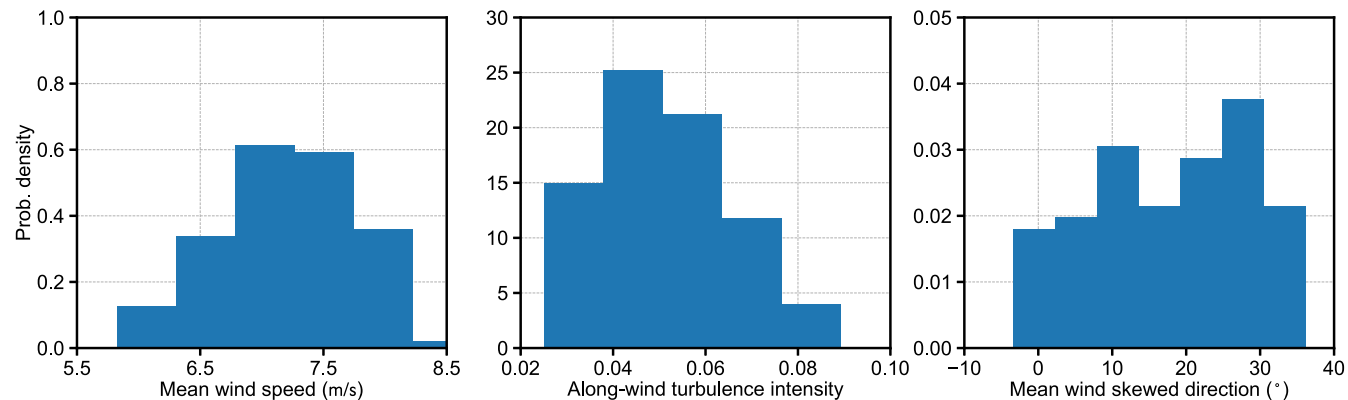


Fig. 11. Mean wind characteristics of selected records.

Strouhal number [40]. The characteristics of vortex-induced vibration are typical single frequency simple harmonic vibration, and the root-mean-square of acceleration response is larger than other vibrations (shown in Fig. 10). Based on the monitoring acceleration of the bridge deck, the two features are employed to distinguish the VIV from other vibrations

$$\left\{ \begin{array}{l} A_{rms} = \sqrt{\frac{1}{N} \sum_{i=1}^N \ddot{y}_i^2} \geq 0.05 \text{ m/s}^2 \\ P_1/P_2 \geq 10 \end{array} \right. \quad (30)$$

where  $A_{rms}$  is the root-mean-square of the measured vertical acceleration response,  $P_1$  is the maximum acceleration amplitude of FFT and  $P_2$  is the second amplitude. Fig. 10 shows the acceleration time history between 20:00:00 and 20:40:00 06/03/2020 of accelerometer

records at the 1/8 span. The first features  $A_{rms} = 0.11 \text{ m/s}^2$  and the second feature  $P_1/P_2 = 13.8$  of the VIV event. The first features  $A_{rms} = 0.01 \text{ m/s}^2$  and the second feature  $P_1/P_2 = 2.5$  of other vibration events. The VIV events can be well distinguished from other vibration responses using the above two features [40].

### 5.2.3. Wind characteristics during vortex-induced vibration events

Using the classification method mentioned above, a total of 100 sets of completed wind characteristics and synchronous acceleration response records were selected. The mean wind characteristics are plotted in Fig. 11 when VIV events occurred. From the distribution of mean wind characteristics, the conditions for VIV are simply summed up into the following three conditions: 10-min mean wind speed in [6, 8.2] m/s, along-wind turbulence intensity in [0.02, 0.09] and 10-min mean

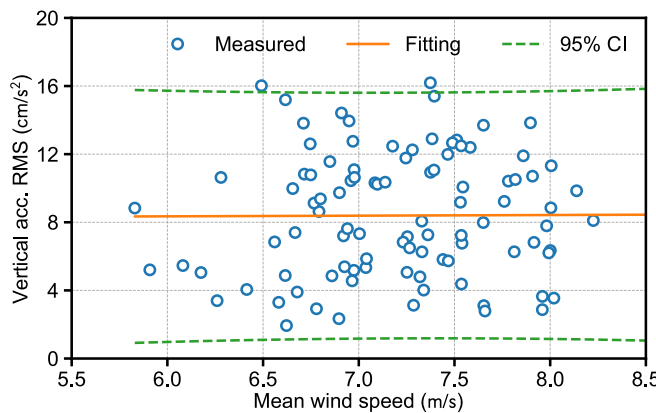


**Fig. 12.** Relationship between the 10-min mean wind speed and vertical acceleration RMS responses.

wind direction in [140, 180]°. According to the wind direction during June 9th, to July 20th, (Fig. 8), an appropriate wind environment is formed for the VIV events during this period. The vibration frequency of the deck is 0.2258 using FFT spectral analysis and the Strouhal number of this deck (Fig. 6) can be simply estimated to be between 0.98 and 1.34.

The scatter and fitting curves between the 10-min mean wind speed and vertical acceleration RMS response are plotted in Fig. 12 and the correlation between them is weak. In other words, the vertical acceleration root-mean-square (RMS) and 10-min mean wind speed have no obvious correlation in the measured data.

### 5.3. Identification result of VEF parameters

After rough processing of the measured wind speed records and acceleration data, the parameters of the VEF can be identified using the Bayesian FFT method mentioned in Section 3, and the flowchart is plotted in Fig. 13. The structural frequency and the aerodynamic stiffness have a significant effect on the VIV response, as well as the structural damping ratio and self-excited damping ratio. To extract  $Y_1$  and  $Y_2$ , the structural frequency and damping ratio should be obtained in advance. The VEF parameter procedure includes two main parts. One part is to identify the dynamic characteristics of the structures by using the nearby ambient excitation acceleration signals of the VIV events to make the calculated structural dynamic characteristics as close as possible to the VIV events. Nearby ambient excitation signals are chosen to reduce the effect of varying structural damping ratios from time to time. The Bayesian FFT identification method of structural modal parameters has been mentioned in some literature [37–39,41] and will not be repeated here. The structural modal shape  $\phi$  can also be treated as a group parameter to be identified using the Bayesian FFT method. However, If only records with measured degree-of-freedom were used to identify the modal shape, the estimated value of modal mass will be very different from the actual value due to the limited number of sensors. This will lead to an inaccurate estimate of generalized lift coefficient  $\hat{C}_L$ . So, the modal shape calculated by the finite element of model are used in this paper. From June 9th, to July 20th, 2020, the modal shape was all second-order symmetric vertical bending when VIV occurred (see Fig. 7). The structural information of Humen Bridge is shown in Table 3.

Fig. 14 shows a typical VIV series at eight points recorded by SHM. Using the VEF parameter identification procedure listed in Fig. 13, the MPVs and c.o.v. values of optimal parameters are listed in Table 4. Given the values of the structural natural frequency and damping ratio,  $Y_1$  and  $Y_2$  were computed to be 1.0091 and 10.4183, respectively. The c.o.v. values of different orders of magnitude reflect the uncertainty,

**Table 3**  
Structural information of Humen Bridge.

Items	Values
Density of air	1.225 kg/m <sup>3</sup>
Width of deck	35.6 m
Mass per meter	$2.4 \times 10^4$ kg/m

**Table 4**  
Identification results of VEF parameters of one series.

Items	$\hat{\omega}$ (rad/s)	$\hat{\xi}$ (%)	$\hat{C}_{L,1}$
Estimate values ( $\hat{\theta}$ )	1.4259	0.13	10.09
$\sigma$	0.0008	0.05	4.50
$\sigma/\hat{\theta}$ (%)	0.06	39.73	44.57

and the identified accuracy of the aerodynamically affected circular frequency was relatively high. To verify the accuracy of the identification parameters, the frequency spectrum acceleration response was obtained by the calculation using the identified VEF parameters and is shown in Fig. 15.

### 5.4. Relationship between VEF parameters and wind characteristics

To evaluate the amplitude of VIV for actual bridges, MPVs are of greater concern. Using the procedure of the Bayesian FFT identification method in Fig. 13, the MPVs of 85 groups of VEF parameters for VIV events were identified. The wind characteristics that may influence the values of the VEF parameters were the 10-min mean wind speed ( $U$ ), wind turbulence intensity ( $I_u$ ), and 10-min mean wind direction ( $\beta$ ). For the extracted VIV events, the matrices of the linear correlation coefficients are plotted in Fig. 16. The triangular points, rectangular points, and circular points denote the correlation between wind characteristics, the correlation between VEF parameters, and the correlation between wind characteristics and VEF parameters, respectively. Examining the figure, the linear correlations between  $U$  and  $I_u$ ,  $U$  and  $Y_1$ ,  $U$  and  $Y_2$ ,  $I_u$  and  $Y_1$  and  $I_u$  and  $Y_2$  are considered significant.

It was previously stated that some of the VEF parameters ( $Y_1$ ,  $Y_2$ ) were also dependent on the 10-min mean wind speed. Consequently, the probability dependence between them is plotted in Fig. 17. Fig. 17(a) shows the relationship between  $Y_1$  and the reduced wind speed  $K = \frac{U}{fD}$ , where  $f$  is the vibration frequency and  $D$  is the width of the girder. The  $Y_1$  related to aerodynamically damping ratio can be equivalent to  $H_1^*$  in flutter derivative. According to Theodorsen function [42],  $H_1^*$  and  $K$  are linearly correlated at low wind speeds. Therefore, the first-order polynomial was employed to fit them:

$$Y_1 = -3.44K + 4.09 \quad (31)$$

The  $Y_2$  related to aerodynamically stiffness can be equivalent to  $H_4^*$  in flutter derivative. According to Theodorsen function [42],  $H_4^*$  and  $K$  are linearly correlated at low wind speeds. The first-order polynomial was employed to fit them:

$$Y_2 = -74.62K + 92.07 \quad (32)$$

The harmonic force coefficient  $\hat{C}_L$  is also a significant parameter when estimating the VIV amplitude at a specific flow condition. When the scatter diagrams were plotted, quadratic correlations were demonstrated between  $K$ ,  $\beta$ , and  $\hat{C}_L$ . The relationship between reduced wind speed  $K$  and harmonic force coefficient  $\hat{C}_L$  is plotted in Fig. 18(a). The linear correlation between  $\hat{C}_L$  and  $K$  is weak when some points with large deviation ( $\hat{C}_L > 100$ ) are excluded. However, it can be noted that in the whole reduced wind speed range,  $\hat{C}_L$  first increases and then decreases with reduced wind speed. This variation trend is consistent with the vibration amplitude within the range of vortex locked wind speed [43], and is also consistent with the variation trend of  $\hat{C}_L$  of cylindrical vortex vibration with reduced wind speed [44]. Fitting with

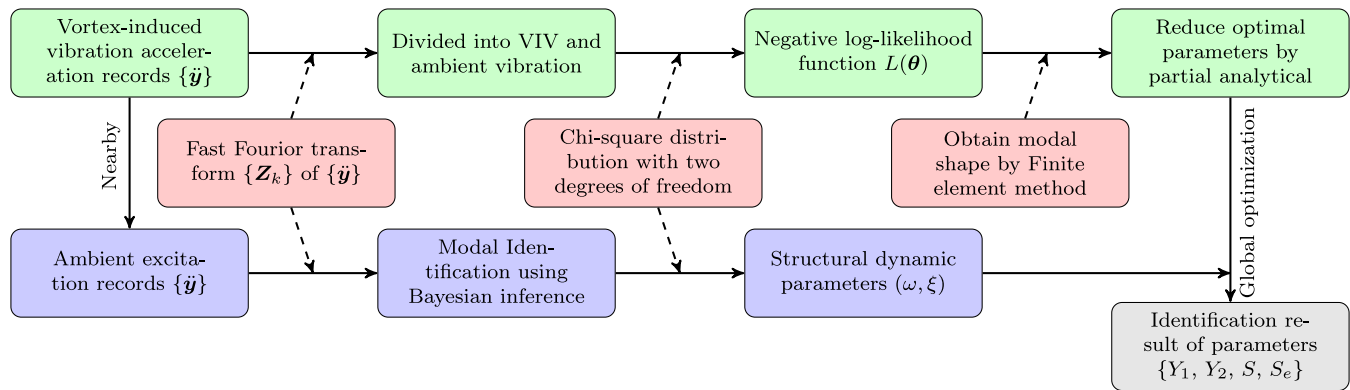


Fig. 13. Flowchart of VEF parameter identification of Humen Bridge.

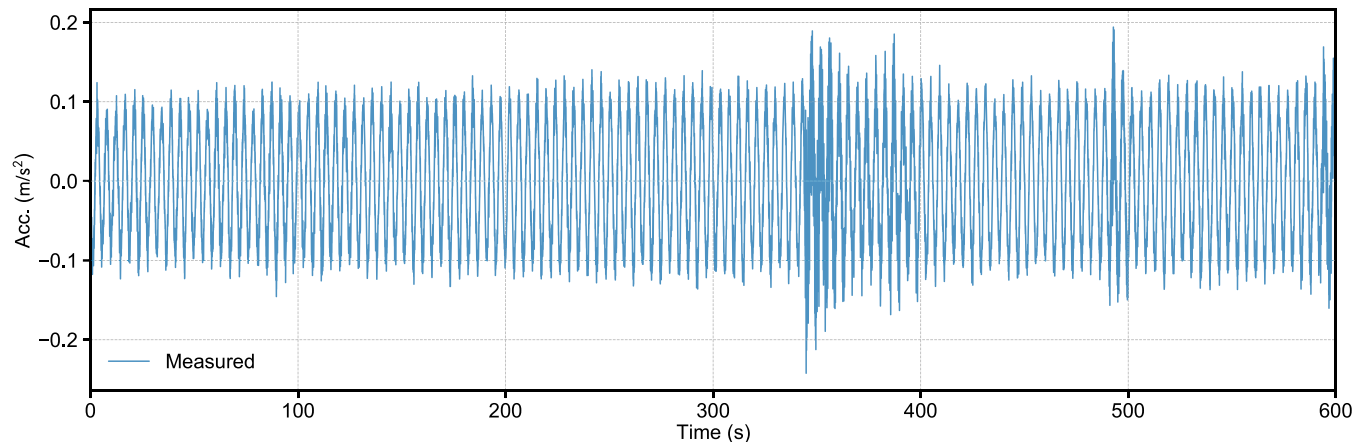


Fig. 14. Time history of eight point acceleration response when VIV.

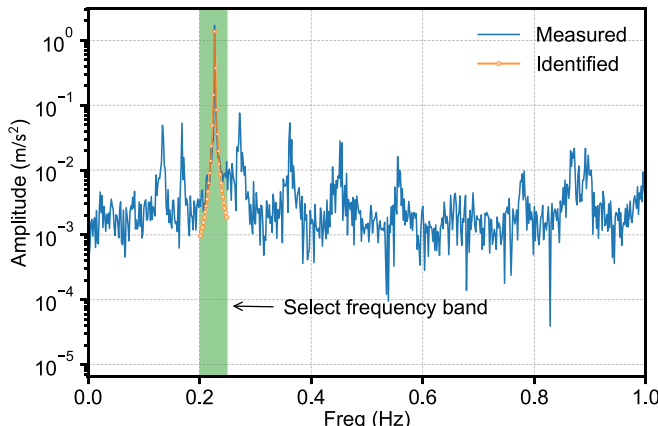


Fig. 15. Identification result of eight point acceleration response on frequency domain when VIV.

a quadratic polynomial, the function is shown in Eq. (33):

$$\hat{C}_L = -866.62K^2 + 1535.40K - 647.66 \quad (33)$$

Considering that the amplitude of the vortex shedding is usually related to the direction of the incoming flow, the scatter point between identified  $\hat{C}_L$  and the angle between the vertical line of the bridge axis and the 10-min mean wind direction ( $\beta - \theta$ ) is drawn in Fig. 18(b). The quadratic polynomial is employed to fit them and the function is given in Eq. (34). From Fig. 18(b), the maximum  $\hat{C}_L$  is obtained when the

incoming flow is at a certain angle with the vertical line of the bridge axis.

$$\hat{C}_L = -92.01(\beta - \theta)^2 + 40.38(\beta - \theta) + 27.38 \quad (34)$$

where  $\beta$  is the 10-min mean wind direction and  $\theta$  is the angle between the bridge axis and the north direction (rad), where  $\theta = 144.7^\circ$ .

To better describe or estimate the harmonic force coefficient  $\hat{C}_L$ , a second-order polynomial function is employed. Fig. 19 shows the scatter and polynomial fitting surface between the harmonic force coefficient  $\hat{C}_L$  and wind characteristics and  $R^2 = 0.1289$ . The fitting polynomial is given by:

$$\hat{C}_L = -715.55K^2 - 64.13(\beta - \theta)^2 + 1270.54K + 27.22(\beta - \theta) - 532.31 \quad (35)$$

### 5.5. Cross validation for the identified results

To estimate the rationality of the fitting polynomial, all the wind characteristic parameters are input into Eq. (31), Eq. (32) and (35) to obtain the corresponding vortex-excited force parameters. Then, Eq. (7) was employed to calculate the responses. The scatters between real amplitudes and estimated amplitudes as shown in Fig. 20. The mean and standard derivation of the difference between them were  $\mu_e = 0.0152$  m and  $\sigma_e = 0.0432$  m, respectively.

To further verify the precision of the identification results, the cross-validation method was used. Four cases were selected, and their wind characteristics and VEF parameters by interpolation are shown in Table 5. Using the VEF parameters, the acceleration response can be calculated as plotted in Fig. 20 and Fig. 21. The estimated values are basically in agreement with the measured values.

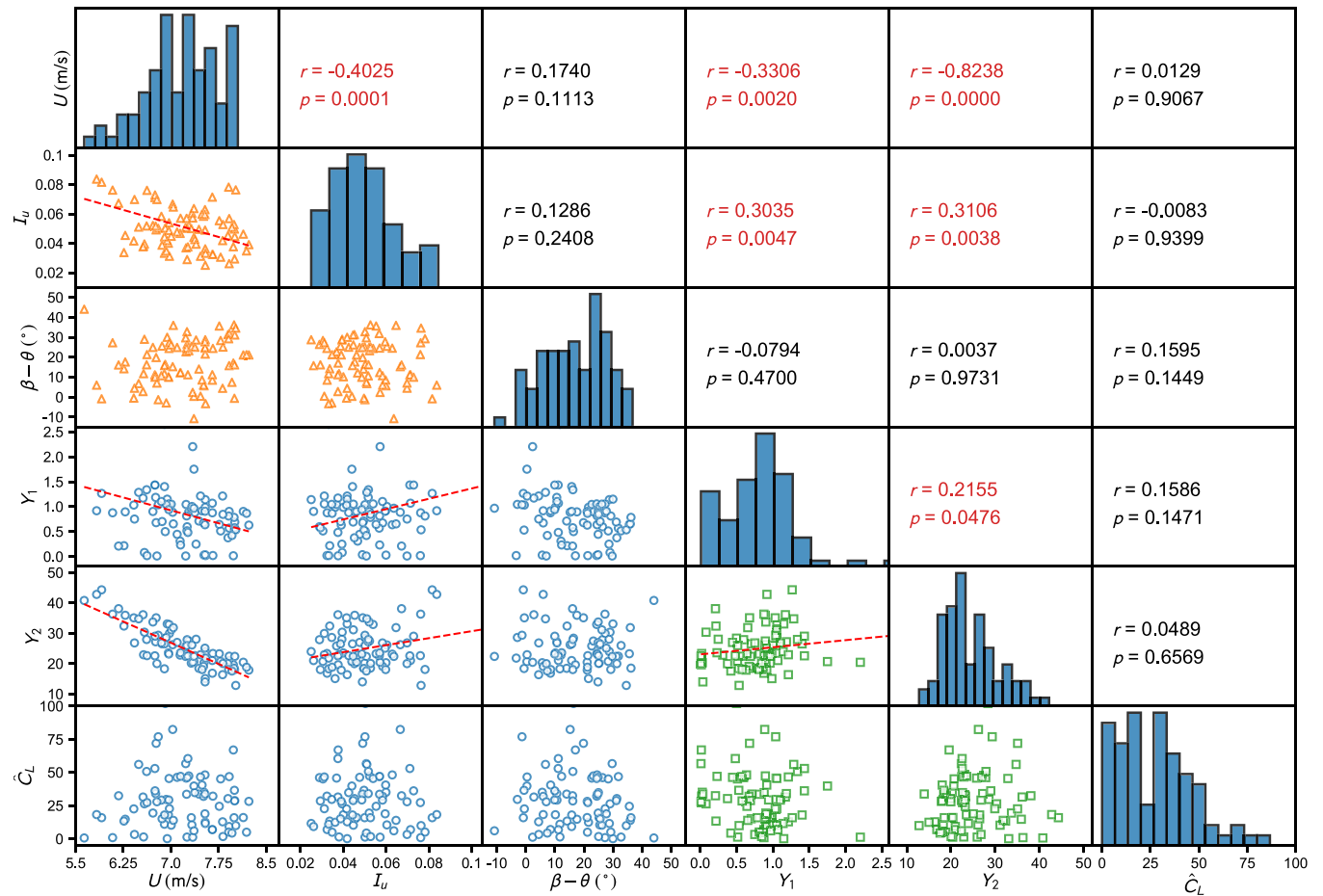
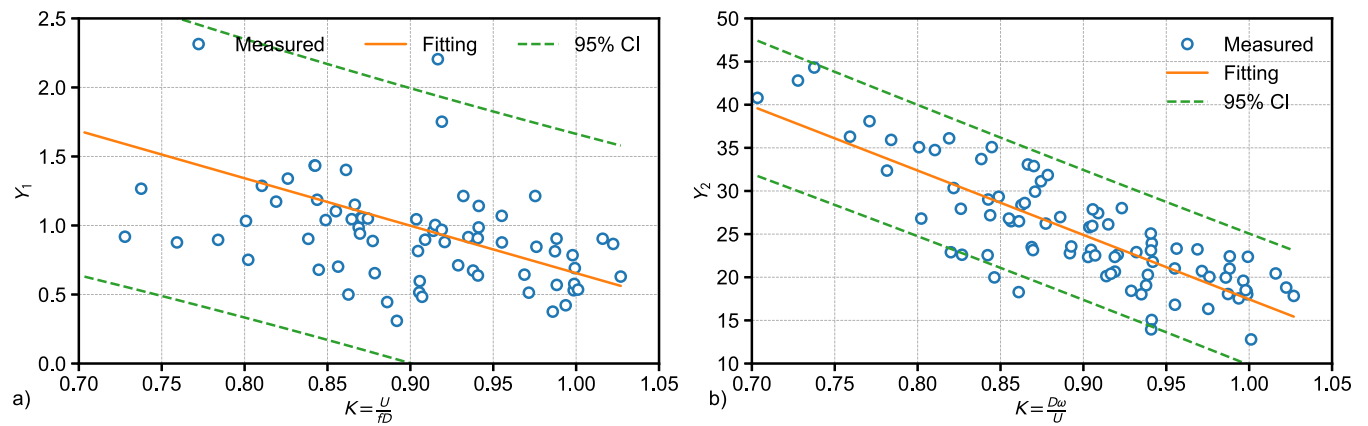


Fig. 16. Scatter plot matrix of the wind characteristics and VEF parameters.

Fig. 17. Relationship between self-excited aerodynamic parameters and reduced wind speed ( $K$ ) (a)  $Y_1$  and  $K$ , (b)  $Y_2$  and  $K$ .

**Table 5**  
Four cross validation cases and their VEF parameters by interpolation.

Item	Wind characteristics		VEF parameters			Results		
	$U$ (m/s)	$\beta$ ( $^{\circ}$ )	$Y_1$	$Y_2$	$\hat{C}_L$	$A_{real}$ (cm)	$A_{cal}$ (cm)	Relative error
Case 1	6.92	157.5	1.05	29.00	33.26	9.49	10.15	6.90%
Case 2	8.14	165.7	0.73	19.19	24.96	13.03	12.04	7.59%
Case 3	6.93	141.7	1.05	28.92	28.86	5.11	5.67	10.95%
Case 4	7.03	159.9	1.02	28.11	33.78	7.14	8.43	18.07%

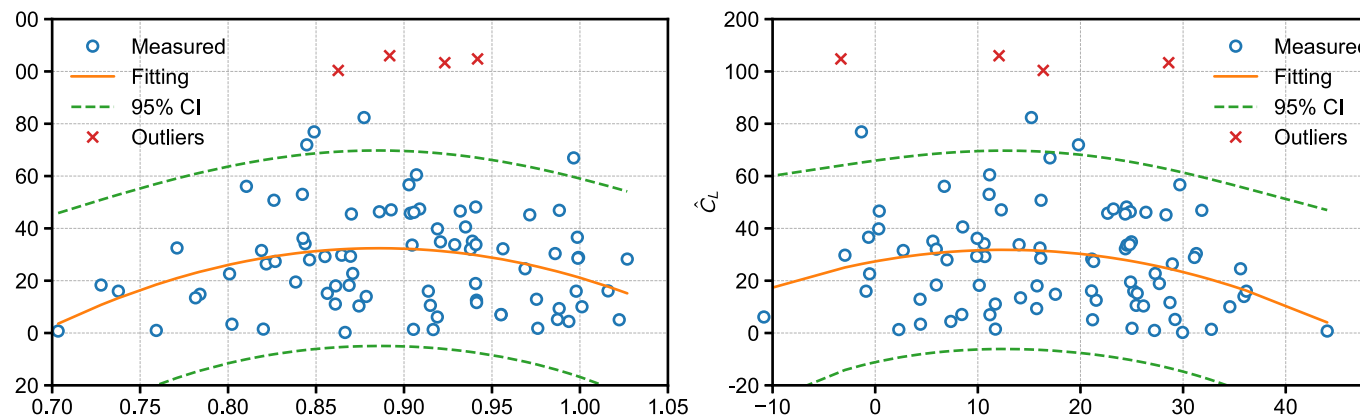


Fig. 18. Relationship between harmonic force coefficient  $\hat{C}_L$  and wind characteristics (a)  $\hat{C}_L$  and  $K$ , (b)  $\hat{C}_L$  and  $(\beta - \theta)$ .

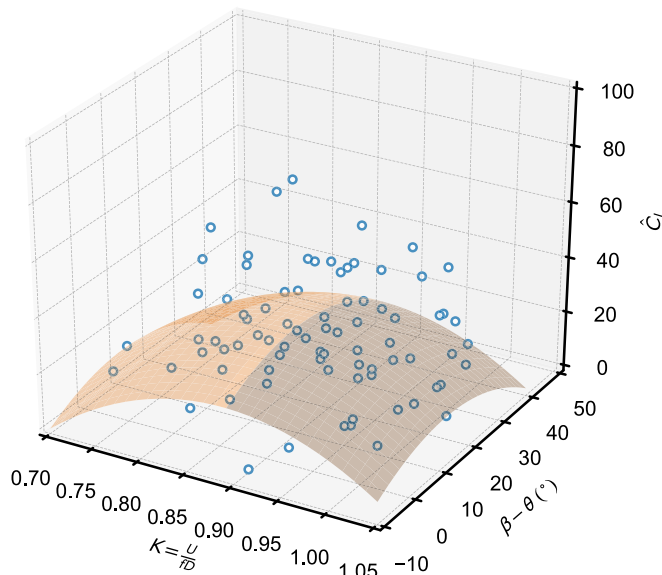


Fig. 19. Scatters and polynomial fitting surface between harmonic force coefficient  $\hat{C}_L$  and wind characteristics.

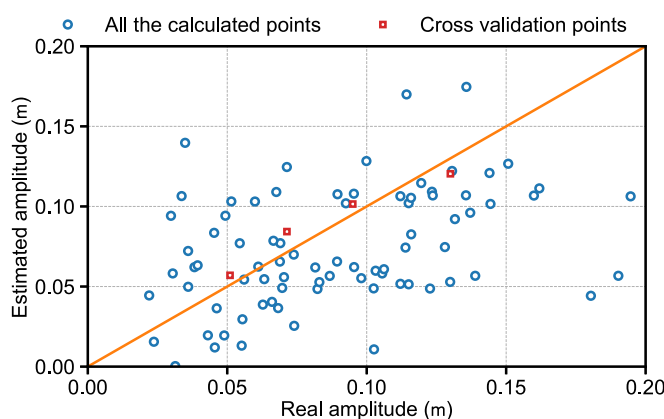


Fig. 20. Scatters between real amplitudes and estimated amplitudes.

## 6. Conclusion

In this paper, the application of the Bayesian FFT method in parametric identification of vortex-excited force (VEF) is described. Considering the turbulence field and measurement noise on prototype monitoring, the identification of vortex-excited force parameters is modeled from the perspective of probability based on the random vibration under ambient excitation. Compared with identifying the VEF in wind tunnel tests, the Bayesian FFT parametric identification method based on on-site measured data can obtain more accurate estimates of vortex-excited force parameters because of the Reynolds number effect in fluid-structure interactions. By introducing a semiempirical VEF model, this method only needs the response data of the bridges and does not need to collect synchronous force or surface pressure signals. The relationship between wind characteristics and VEF parameters was explored. There is a linear relationship between the 10-min mean wind speed and aerodynamic stiffness, so also between the 10-min mean wind speed and aerodynamic damping ratio. The harmonic force coefficient had a quadratic correlation with the 10-min mean wind speed and wind direction when VIV events occurred. Finally, cross-validation was employed to estimate the identified results and the Bayesian FFT method performed well in VEF parametric identification.

## CRediT authorship contribution statement

**Peng Liu:** Writing – original draft, Conceptualization, Formal analysis, Investigation, Methodology, Validation, Visualization. **Xiaolei Chu:** Methodology. **Wei Cui:** Conceptualization, Supervision, Writing – review & editing, Funding acquisition. **Lin Zhao:** Supervision, Funding acquisition. **Yaojun Ge:** Funding acquisition.

## Declaration of competing interest

The authors declare that they have no known competing financial interests or personal relationships that could have appeared to influence the work reported in this paper.

## Acknowledgments

The authors gratefully acknowledge the support of National Natural Science Foundation of China (52078383, 52008314), Independent subject of State Key Lab of Disaster Reduction in Civil Engineering (SLDRCE19-B-11) and National Key Research and Development Program of China (2021YFF0502200). Any opinions, findings and conclusions are those of the authors and do not necessarily reflect the reviews of the above agencies.

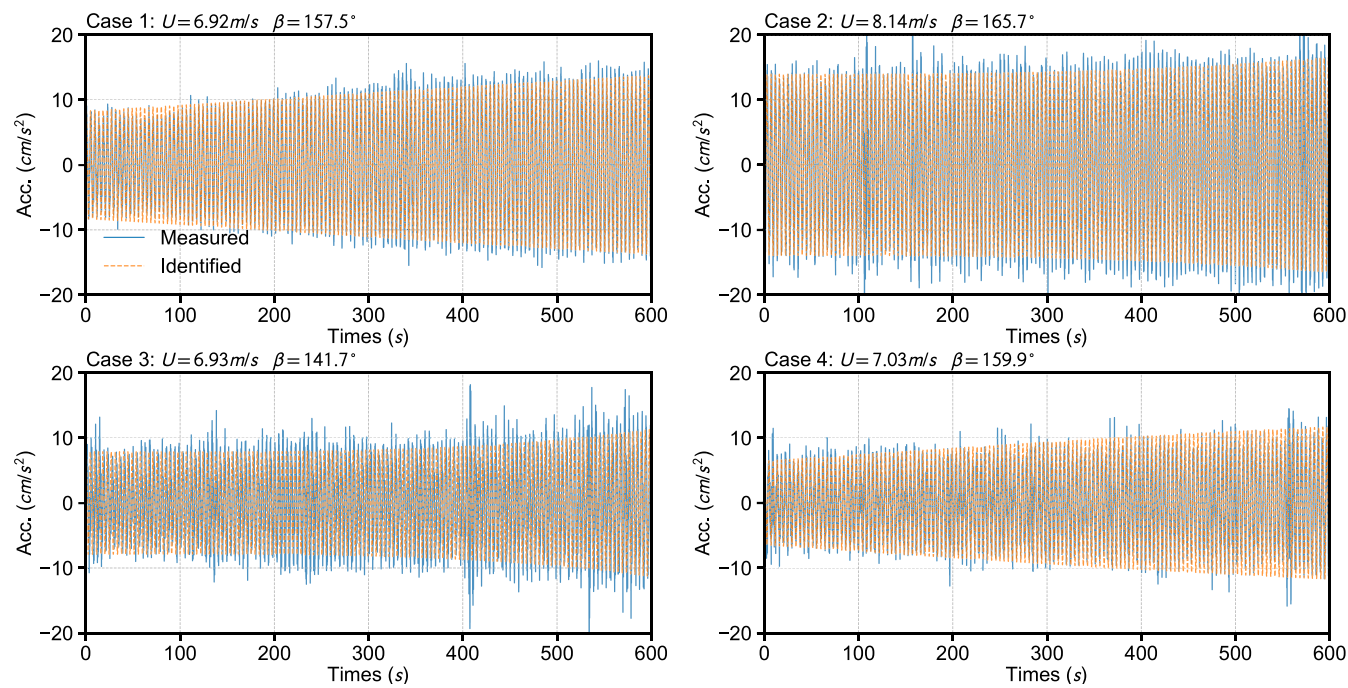


Fig. 21. Cross validation using VEF parameters obtained by fitting polynomial interpolation.

## References

- [1] Cui W, Caracoglia L. A unified framework for performance-based wind engineering of tall buildings in hurricane-prone regions based on lifetime intervention-cost estimation. *Struct Saf* 2018;73:75–86.
- [2] Hu C, Zhao L, Ge Y. Time-frequency evolutionary characteristics of aerodynamic forces around a streamlined closed-box girder during vortex-induced vibration. *J Wind Eng Ind Aerodyn* 2018;182:330–43.
- [3] Kumarasena T, Scanlan R, Ehsan F. Wind-induced motions of deer isle bridge. *J Struct Eng* 1991;117(11):3356–74.
- [4] Larsen A, Esdahl S, Andersen JE, Vejrum T. Storebælt suspension bridge–vortex shedding excitation and mitigation by guide vanes. *J Wind Eng Ind Aerodyn* 2000;88(2–3):283–96.
- [5] Hwang YC, Kim S, Kim H-K. Cause investigation of high-mode vortex-induced vibration in a long-span suspension bridge. *Struct Infrastruct Eng* 2020;16(1):84–93.
- [6] Li H, Laima S, Ou J, Zhao X, Zhou W, Yu Y, et al. Investigation of vortex-induced vibration of suspension bridge with two separated steel box girders based on field measurements. *Eng Struct* 2011;33(6):1894–907.
- [7] Zhao L, Cui W, Shen X, Xu S, Ding Y, Ge Y. A fast on-site measure-analyze-suppress response to control vortex-induced-vibration of a long-span bridge. In: *Structures*. 35, Elsevier; 2022, p. 192–201.
- [8] Simiu E, Scanlan RH. Wind effects on structures: fundamentals and applications to design. John Wiley New York; 1996.
- [9] Larsen A. A generalized model for assessment of vortex-induced vibrations of flexible structures. *J Wind Eng Ind Aerodyn* 1995;57(2–3):281–94.
- [10] Zhu L-D, Meng X-L, Guo Z-S. Nonlinear mathematical model of vortex-induced vertical force on a flat closed-box bridge deck. *J Wind Eng Ind Aerodyn* 2013;122:69–82.
- [11] Wu T, Kareem A. Vortex-induced vibration of bridge decks: Volterra series-based model. *J Eng Mech* 2013;139(12):1831–43.
- [12] Xu K, Zhao L, Ge Y. Reduced-order modeling and calculation of vortex-induced vibration for large-span bridges. *J Wind Eng Ind Aerodyn* 2017;167:228–41.
- [13] Liu P, Zhao L, Fang G, Ge Y. Explicit polynomial regression models of wind characteristics and structural effects on a long-span bridge utilizing onsite monitoring data. *Struct Control Health Monit* 2021;28(5):e2705.
- [14] Mao J-X, Wang H, Feng D-M, Tao T-Y, Zheng W-Z. Investigation of dynamic properties of long-span cable-stayed bridges based on one-year monitoring data under normal operating condition. *Struct Control Health Monit* 2018;25(5):e2146.
- [15] Zhang J, Zhou L, Tian Y, Yu S, Zhao W, Cheng Y. Vortex-induced vibration measurement of a long-span suspension bridge through noncontact sensing strategies. *Comput-Aided Civ Infrastruct Eng* 2021.
- [16] Spencer R. A time domain modal vibration test technique. *Shock Vib Digest* 1974;6(6):60.
- [17] Ruzzene M, Fasana A, Garibaldi L, Piombo B. Natural frequencies and dampings identification using wavelet transform: application to real data. *Mech Syst Signal Process* 1997;11(2):207–18.
- [18] Lardies J, Gouttebroze S. Identification of modal parameters using the wavelet transform. *Int J Mech Sci* 2002;44(11):2263–83.
- [19] Wu Y, Chen X, Wang Y. Identification of linear and nonlinear flutter derivatives of bridge decks by unscented Kalman filter approach from free vibration or stochastic buffeting response. *J Wind Eng Ind Aerodyn* 2021;214:104650.
- [20] Yan W-J, Ren W-X. Operational modal parameter identification from power spectrum density transmissibility. *Comput-Aided Civ Infrastruct Eng* 2012;27(3):202–17.
- [21] Vanik MW, Beck JL, Au S-K. Bayesian probabilistic approach to structural health monitoring. *J Eng Mech* 2000;126(7):738–45.
- [22] Beck JL. Bayesian system identification based on probability logic. *Struct Control Health Monit* 2010;17(7):825–47.
- [23] Au S-K, Zhang F-L, Ni Y-C. Bayesian operational modal analysis: theory, computation, practice. *Comput Struct* 2013;126:3–14.
- [24] Yuen K-V. Bayesian methods for structural dynamics and civil engineering. John Wiley & Sons; 2010.
- [25] Yuen K-V, Katafygiotis LS. Bayesian time-domain approach for modal updating using ambient data. *Probab Eng Mech* 2001;16(3):219–31.
- [26] Chu X, Cui W, Liu P, Zhao L, Ge Y. Bayesian spectral density approach for identification of bridge section's flutter derivatives operated in turbulent flow. *Mech Syst Signal Process* 2022;170:108782.
- [27] Yan W-J, Feng Z-Q, Yang W, Yuen K-V. Bayesian inference for the dynamic properties of long-span bridges under vortex-induced vibration with Scanlan's model and dense optical flow scheme. *Mech Syst Signal Process* 2022;174:109078.
- [28] Yuen K-V, Katafygiotis LS. Bayesian fast Fourier transform approach for modal updating using ambient data. *Adv Struct Eng* 2003;6(2):81–95.
- [29] Zhang F-L, Ni Y-C, Au S-K, Lam H-F. Fast Bayesian approach for modal identification using free vibration data, Part I—Most probable value. *Mech Syst Signal Process* 2016;70:209–20.
- [30] Au S-K. Fast Bayesian FFT method for ambient modal identification with separated modes. *J Eng Mech* 2011;137(3):214–26.
- [31] Au S-K. Fast Bayesian ambient modal identification in the frequency domain, Part II: Posterior uncertainty. *Mech Syst Signal Process* 2012;26:76–90.
- [32] Goswami I, Scanlan RH, Jones NP. Vortex-induced vibration of circular cylinders. II: new model. *J Eng Mech* 1993;119(11):2288–302.
- [33] Vickery B, Basu R. Across-wind vibrations of structures of circular cross-section. Part I. Development of a mathematical model for two-dimensional conditions. *J Wind Eng Ind Aerodyn* 1983;12(1):49–73.
- [34] Smith IJ. Wind induced dynamic response of the wye bridge. *Eng Struct* 1980;2(4):202–8.
- [35] Chen G-W, Beskyroun S, Omensetter P. Experimental investigation into amplitude-dependent modal properties of an eleven-span motorway bridge. *Eng Struct* 2016;107:80–100.
- [36] Owen JS, Vann AM, Davies JP, Blakeborough A. The prototype testing of Kessock Bridge: response to vortex shedding. *J Wind Eng Ind Aerodyn* 1996;60(none):91–108.

- [37] Yuen K-V. Recent developments of Bayesian model class selection and applications in civil engineering. *Struct Saf* 2010;32(5):338–46.
- [38] Yuen K-V, Katafygiotis LS. Substructure identification and health monitoring using noisy response measurements only. *Comput-Aided Civ Infrastruct Eng* 2006;21(4):280–91.
- [39] Au S-K. Fast Bayesian ambient modal identification in the frequency domain, Part I: Posterior most probable value. *Mech Syst Signal Process* 2012;26:60–75.
- [40] Li S, Laima S, Li H. Cluster analysis of winds and wind-induced vibrations on a long-span bridge based on long-term field monitoring data. *Eng Struct* 2017;138:245–59.
- [41] Chu X, Cui W, Zhao L, Ge Y. Life-cycle assessment of long-span bridge's wind resistant performance considering multisource time-variant effects and uncertainties. *J Struct Eng* 2022;148(8):04022092.
- [42] Scanlan RH. Problematics in formulation of wind-force models for bridge decks. *J Eng Mech* 1993;119(7):1353–75.
- [43] Zhang M, Wu T, Xu F. Vortex-induced vibration of bridge decks: describing function-based model. *J Wind Eng Ind Aerodyn* 2019;195:104016.
- [44] Sarpkaya T. Vortex shedding and resistance in harmonic flow about smooth and rough circular cylinders at high Reynolds numbers. Tech. rep., Naval Postgraduate School Monterey CA; 1976.